



Milliwatt-threshold visible–telecom optical parametric oscillation using silicon nanophotonics

XIYUAN LU,^{1,2,8} GREGORY MOILLE,^{1,6} ANSHUMAN SINGH,^{1,2} QING LI,^{1,2,3} DARON A. WESTLY,¹ ASHUTOSH RAO,^{1,7} SU-PENG YU,^{4,5} TRAVIS C. BRILES,^{4,5} SCOTT B. PAPP,^{4,5} AND KARTIK SRINIVASAN^{1,6,*}

¹Microsystems and Nanotechnology Division, Physical Measurement Laboratory, National Institute of Standards and Technology, Gaithersburg, Maryland 20899, USA

²Institute for Research in Electronics and Applied Physics and Maryland Nanocenter, University of Maryland, College Park, Maryland 20742, USA

³Department of Electrical and Computer Engineering, Carnegie Mellon University, Pittsburgh, Pennsylvania 15213, USA

⁴Time and Frequency Division, Physical Measurement Laboratory, National Institute of Standards and Technology, Boulder, Colorado 80305, USA

⁵Department of Physics, University of Colorado, Boulder, Colorado 80309, USA

⁶Joint Quantum Institute, NIST/University of Maryland, College Park, Maryland 20742, USA

⁷Department of Chemistry and Biochemistry, University of Maryland, College Park, Maryland 20742, USA

⁸e-mail: xiyuan.lu@nist.gov

*Corresponding author: kartik.srinivasan@nist.gov

Received 23 September 2019; revised 18 November 2019; accepted 19 November 2019 (Doc. ID 378552); published 19 December 2019

The on-chip creation of coherent light at visible wavelengths is crucial to field-level deployment of spectroscopy and metrology systems. Although on-chip lasers have been implemented in specific cases, a general solution that is not restricted by limitations of specific gain media has not been reported, to the best of our knowledge. Here, we propose creating visible light from an infrared pump by widely separated optical parametric oscillation (OPO) using silicon nanophotonics. The OPO creates signal and idler light in the 700 nm and 1300 nm bands, respectively, with a 900 nm pump. It operates at a threshold power of (0.9 ± 0.1) mW, over $50\times$ smaller than other widely separated microcavity OPO works, which have been reported only in the infrared. This low threshold enables direct pumping without need of an intermediate optical amplifier. We further show how the device design can be modified to generate 780 nm and 1500 nm light with a similar power efficiency. Our nanophotonic OPO shows distinct advantages in power efficiency, operation stability, and device scalability, and is a major advance towards flexible on-chip generation of coherent visible light.

<https://doi.org/10.1364/OPTICA.6.001535>

1. INTRODUCTION

On-chip generation of coherent light at visible frequencies is critical for miniaturization and field-level deployment for spectroscopy and metrology, e.g., wavelength-stabilized reference lasers based on atomic vapors [1] and optical atomic clocks [2]. One approach is to develop on-chip lasers directly using III–V semiconductors [3], but the wavelength coverage is limited by the available gain media and requires nontrivial heterogeneous integration to be compatible with a silicon chip. Another approach is to use nonlinear optics to create light at new frequencies from existing lasers. There are many second/third-order ($\chi^{(2)}/\chi^{(3)}$) nonlinear optical processes for this purpose, including optical parametric oscillation (OPO), second/third-harmonic generation (SHG/THG), sum frequency generation (SFG), and stimulated four-wave mixing/optical parametric amplification (StFWM/OPA) [4,5]. Among these processes, OPO is uniquely suitable to generate coherent light over a wide spectral range, because the generated light is not limited to harmonics of pump frequencies (unlike SHG/THG), and only one

pump laser is required (unlike SFG/StFWM/OPA). Historically, $\chi^{(2)}$ OPO has been particularly efficient in creating coherent light across wide spectral ranges. Half a century ago, coherent OPO light from 970 nm to 1150 nm was generated by a 529 nm pump laser in a LiNbO₃ crystal [6]. Later, the OPO signal wavelength was brought into the visible (from 537 nm to 720 nm) by a 308 nm pump laser in a BaB₂O₄ crystal [7]. Nowadays, $\chi^{(2)}$ OPO systems have become a laboratory workhorse tool in the generation of coherent, tunable visible light, particularly when pumped by a Ti:sapphire laser [8]. However, nanophotonic implementations of OPO that can reach visible wavelengths are still lacking.

In this work, we report a nanophotonic $\chi^{(3)}$ OPO for on-chip visible light generation. We use $\chi^{(3)}$ rather than $\chi^{(2)}$ for two important reasons. First, $\chi^{(3)}$ processes, unlike $\chi^{(2)}$ processes, are naturally compatible with silicon photonics. Second, as the $\chi^{(3)}$ OPO consumes two pump photons for each generated signal/idler pair, visible wavelengths can be reached through an easily available infrared pump laser, in contrast to a $\chi^{(2)}$ OPO, which needs a UV

pump laser. Although ideas for how to achieve widely separated $\chi^{(3)}$ OPO have been demonstrated in photonic-crystal-fiber-based systems [9,10] and then introduced to silicon nanophotonics theoretically over a decade ago [11], because of the challenging dispersion engineering requirements, such nanophotonic OPO has not been experimentally demonstrated. This is in contrast to other wide-band nonlinear processes, e.g., nanophotonic SHG/THG, which have been extensively reported [12–18]. Recently, widely separated OPO has been achieved in whispering-gallery mode (WGM) platforms with larger footprints, including crystalline MgF_2 microcavities [19–21] and SiO_2 microtoroids [15], but the threshold powers are relatively large, and the spectra of the OPO output have been restricted to the infrared.

To demonstrate nanophotonic visible–telecom OPO, we use the silicon nitride (Si_3N_4) platform, whose advantageous characteristics for silicon-based nonlinear nanophotonics [22], including octave-spanning frequency combs [23–25], frequency conversion/spectral translation [26–28], entanglement generation [29], and clustered frequency comb generation [30,31], have by now been well established. Here we show, for the first time, on-chip OPO with signal and idler at visible and telecom frequencies, e.g., 419.8 THz (714.6 nm) and 227.8 THz (1316.9 nm), respectively. The OPO process is power efficient due to nanophotonic confinement and strong spatial mode overlap, and has an ultra-low threshold power of (0.9 ± 0.1) mW. In contrast to recent microresonator OPO works that use between 50 mW and 380 mW of pump power to achieve widely separated signal and idler in the infrared [15,19–21], our devices use only milliwatt-level power, without intermediate optical amplifiers, to achieve widely separated signal and idler in the visible and telecom, respectively. We further show that the OPO frequencies can be readily controlled by changing the device geometry. In particular, we demonstrate OPO with signal and idler at 383.9 THz (781.4 nm) and 202.1 THz (1484 nm), respectively, by pumping at 293.0 THz (1024 nm). This signal wavelength is suitable for rubidium vapor, and the pump wavelength is accessible from compact semiconductor chip lasers.

2. DESIGN PRINCIPLES

Our OPO devices are based on cavity-enhanced degenerate FWM (dFWM), which requires conservation of both momentum and energy for the interacting optical modes [32]. For the same mode family, momentum conservation is simplified to conservation of the azimuthal mode number, i.e., $\Delta m = m_s + m_i - 2m_p = 0$, where the subscripts s , i , p denote signal, idler, and pump, respectively. Energy conservation requires the central frequencies of the cavity modes to have a mismatch ($\Delta\nu = \nu_s + \nu_i - 2\nu_p$) within the cavity linewidths, i.e., $|\Delta\nu| < \nu_k/Q_k$, where $k = s, i, p$, and Q_k is the loaded quality factor for the k mode. We note that achieving such phase and frequency matching across visible and telecom bands has been demonstrated recently in silicon nanophotonics only for photon-pair generation [29] and spectral translation [28], where a mode-splitting approach [33] enables the identification of specific azimuthal modes separated by hundreds of THz. We employ a similar approach here, focusing on fundamental transverse electric (TE1) modes only, which have high- Q , strong modal confinement (\bar{V}), and good mode overlap (η). These attributes are essential for achieving low-threshold operation, as discussed in Supplement 1.

However, the above design principles do not guarantee that the targeted wide-band OPO process will occur. Critically, the targeted process also has to win over all other competing processes that are matched in phase and frequency, including OPO in the pump band [28,29], clustered frequency combs in the signal and idler bands [15,20,30,31], and other nonlinear processes (e.g., stimulated Raman scattering [19] and THG [15]). For example, recent work reporting telecom-to-visible spectral translation via stimulated dFWM did not exhibit widely separated OPO, because without the seed telecom light, close-to-pump OPO processes dominate [28]. Thus, unlike previous work in wide-band silicon nonlinear nanophotonics [23–26,28,29], visible–telecom OPO faces a more stringent requirement not only on enhancing the process of interest, but also on suppressing all competing processes at the same time.

In particular, OPO in the pump band can be suppressed if the pump modes are in the normal dispersion regime [11], which corresponds to a negative dispersion parameter (D). $D = -\frac{\lambda}{c} \frac{d^2\bar{n}}{d\lambda^2}$, where c , λ , and \bar{n} represent the speed of light, vacuum wavelength, and effective mode index, respectively [5]. $D < 0$ is equivalent to $\Delta\nu < 0$ when the signal and idler modes are near the pump mode. Therefore, we need to design the device to have $\Delta\nu < 0$ when signal and idler are near the pump, and $\Delta\nu = 0$ when signal and idler are widely separated.

3. NUMERICAL SIMULATIONS

We use the aforementioned design principles to guide numerical simulations for the widely separated OPO. Figure 1(b) shows a cross-sectional view of the microring. The Si_3N_4 core has a rectangular cross section, described by ring width (RW), thickness (H), and ring radius (RR). We use these parameters to tailor the geometric contribution to the dispersion. We note that self-/cross-phase modulation is negligible in our device, so that we can use the natural cavity frequencies to design our OPO (see Supplement 1).

Figure 1(c) shows the dispersion parameter of a device with $RW = 1160$ nm, $H = 510$ nm, and $RR = 23$ μm , where the zero-dispersion frequency (ZDF) is at ≈ 321 THz. The dispersion is anomalous for smaller frequencies and normal for larger frequencies. The frequency mismatch ($\Delta\nu$) is plotted [Fig. 1(d)] with pump frequency (ν_p) ranging from 314 THz to 328 THz. When $\nu_p = 322$ THz, nearby modes show an overall small normal dispersion, and there are two widely separated mode pairs that are frequency matched ($\Delta\nu = 0$). In contrast, larger values of ν_p have large normal dispersion and do not lead to widely separated OPO. Smaller ν_p may allow widely separated OPO (e.g., 319 THz case), but the anomalous dispersion around the pump results in several close-band competitive OPO processes, making widely separated OPO unavailable in general.

We also simulate devices that have different RW but the same RR and H , with the dispersion plotted in Fig. 2(a). When RW increases from 1140 nm to 1160 nm, the ZDF red shifts from 325 THz to 321 THz, remaining within our laser scanning range. We thus have a prescription for geometries to experimentally observe the transition from close-band to widely separated OPO processes. For details regarding the parametric sensitivity in dispersion engineering, please refer to Supplement 1.

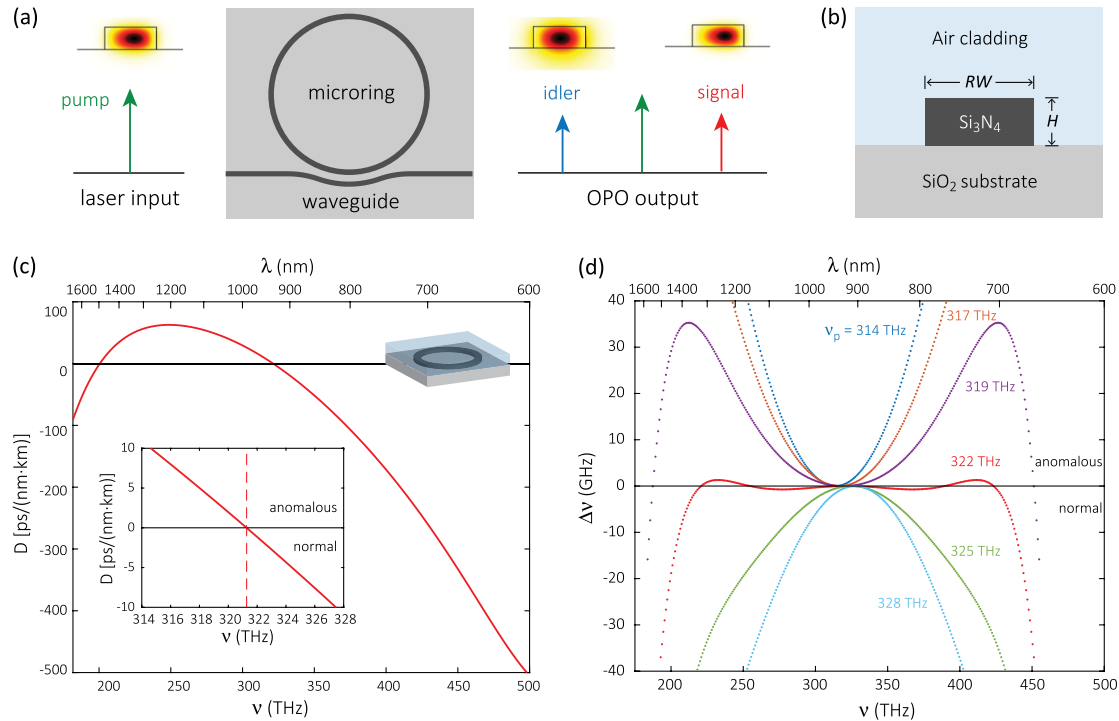


Fig. 1. Design of a nanophotonic visible-telecom optical parametric oscillator. (a) Schematic indicating that the microring device uses cavity-enhanced degenerate four-wave mixing (dFWM) to generate signal and idler light that have frequencies widely separated from the input pump. All interacting modes (pump, signal, and idler) are fundamental transverse-electric modes (TE₁), with their dominant electric field components shown in insets. The input pump and the output signal and idler are all coupled with the same waveguide in this scheme. (b) Cross-section view of the microring shows the air cladding and silicon dioxide substrate, and two key geometric parameters, ring width (RW) and height (H). These two parameters, together with the ring outer radius (RR), unambiguously determine the microring dispersion. (c) Dispersion curve (D) of a typical geometry, with $RR = 23 \mu\text{m}$, $RW = 1160 \text{ nm}$, and $H = 510 \text{ nm}$. $D = 0$ when the pump frequency ν_p is $\approx 321.7 \text{ THz}$ (932.5 nm), as shown in the zoomed-in inset. The dispersion is anomalous ($D > 0$) when ν_p is smaller, and normal ($D < 0$) when ν_p is larger. (d) Frequency mismatch ($\Delta\nu$) for dFWM for the geometry in (c) at various values of ν_p . When the pump is slightly normal at 322 THz (red), there are two cases in which signal and idler modes are phase/frequency matched, with both suitable for widely separated OPO. $\Delta\nu$ is calculated for specific mode number (m) sets, because dFWM requires the phase-matching condition to be satisfied, i.e., $m_s + m_i = 2m_p$. The mode frequency for each mode number is calculated for the geometry in (c) by the finite-element method.

4. EXPERIMENTAL MEASUREMENTS

We fabricate devices (see Supplement 1) with fixed H and varying RW , and characterize them as a function of ν_p near the ZDF. The results are summarized in Figs. 2(b) and 2(c). The output OPO spectra are recorded by an optical spectrum analyzer (OSA), while the pump is scanned for modes that transit from anomalous to normal dispersion, with an example in Fig. 2(c) for fixed $RW = 1150 \text{ nm}$. The OPO signal and idler frequencies for all RW and ν_p are then plotted in Fig. 2(b). ν_p for OPO with the widest separation red shifts from 327.8 THz ($RW = 1160 \text{ nm}$) to 325.7 THz ($RW = 1150 \text{ nm}$) and 323.8 THz ($RW = 1140 \text{ nm}$), following the shift in device dispersion. Focusing again on the $RW = 1150 \text{ nm}$ spectra for several different ν_p [Fig. 2(c)], we clearly observe the trend predicted previously when tuning ν_p from anomalous to normal. When the pump dispersion is anomalous, OPO signal and idler bands are closely spaced around the pump [top panel in Fig. 2(c)]. When the pump dispersion is slightly normal, the OPO signal and idler have increasingly large spectral separation as ν_p increases [second to fourth panels in Fig. 2(c)]. However, when the pump dispersion is too normal, no widely separated OPO is observed, and only very close-band OPO is seen [bottom panel in Fig. 2(c)]. The $RW = 1160 \text{ nm}$ device [red in Fig. 2(b)] has a similar trend but fewer pumping modes in the transition to the slightly normal

region. This trend agrees with the prediction in Fig. 1(d), although the experimental ν_p is 2 THz larger than predicted, which is likely due to uncertainties in device fabrication.

We focus on the $RW = 1160 \text{ nm}$ device and study its power dependence at $\nu_p = 322 \text{ THz}$ in Fig. 3. The OPO signal and idler have a spectral separation that is too large for a single waveguide [Fig. 1(a)] to out-couple both frequencies efficiently. We therefore use two waveguides to separate the coupling tasks, as shown in Fig. 3(a). The bottom pulley waveguide couples the pump and signal light together, while being cutoff at telecom wavelengths (Supplement 1). The top waveguide couples telecom light efficiently, but does not couple the pump and signal light due to a limited spatial overlap that prevents effective evanescent coupling. The combined coupling geometry is designed to have coupling $Q = (1 - 2) \times 10^6$ for pump, signal, and idler modes. In experiment, we verify that the fabricated device has intrinsic $Q = (2 - 3) \times 10^6$ and loaded $Q \approx 1 \times 10^6$ for TE₁ modes in the pump band, which corresponds to loaded cavity linewidths of $\approx 300 \text{ MHz}$. With such high Q , the device shows large thermal bistability at milliwatt pump powers, as shown in Fig. 3(b). For each pump power, we situate the pump detuning near the dip of the cavity resonance and measure the generated OPO spectrum. Three representative spectra are shown in Fig. 3(e), with pump detuning indicated by the open circles in Fig. 3(b). For 1 mW pump power

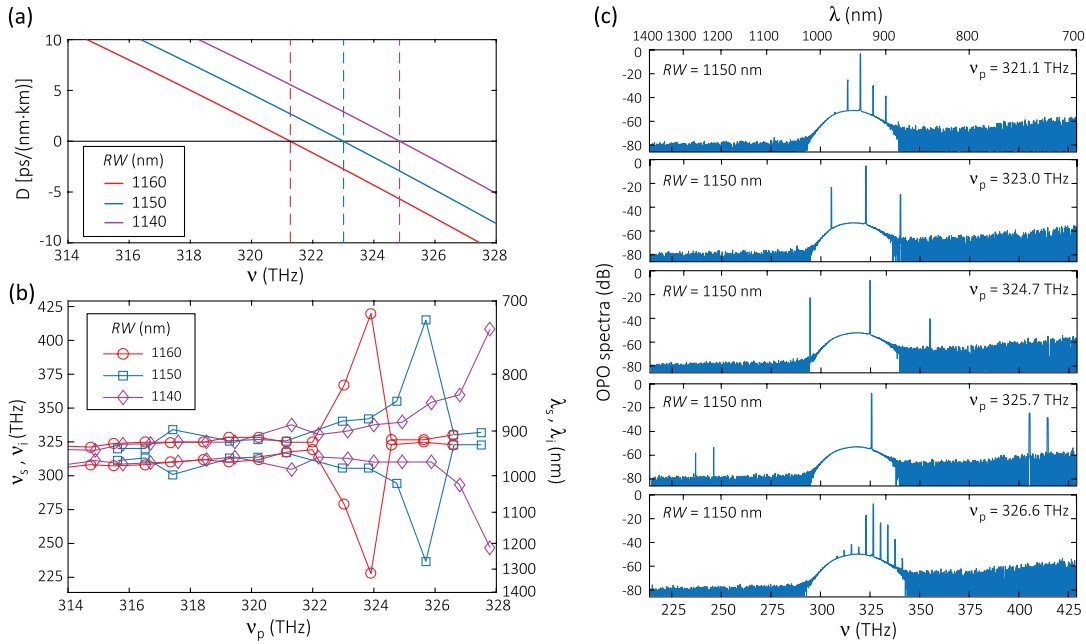


Fig. 2. OPO frequencies critically depend on ring width (RW) and pumping frequency (ν_p). (a) Simulated dispersion (D) curves for different RW , with other parameters specified in the caption of Fig. 1. The zero-dispersion frequency (ZDF) blue shifts with decreasing RW . (b) Experimentally recorded OPO output (signal and idler) frequencies (left axis, ν_s and ν_i) and wavelengths (right axis, λ_s and λ_i) of the aforementioned geometries when ν_p is varied around the ZDF. Widely separated OPO occurs when the dispersion is slightly normal, as suggested by Fig. 1, because potential close-band OPO processes are inhibited. (c) OPO spectra for the $RW = 1150$ nm device when ν_p is varied. When scanning ν_p from a mode in the anomalous region to one in the normal region, the spectral separation of the OPO signal and idler increases from 9 THz to 37 THz, 61 THz, and 178 THz, and finally decreases to 7 THz (from top to bottom). On the y axis, 0 dB is referenced to 1 mW, i.e., dBm.

at $\nu_p = 323.8$ THz (926.5 nm), the top panel in Fig. 3(e) shows that a widely separated OPO is generated with signal at 419.8 THz (714.6 nm) and idler at 227.8 THz (1317 nm). The signal–idler separation is 192 THz, comparable to the largest reported value for WGM resonators (≈ 230 THz), where the idler frequency was inferred [21] (signal and idler were both in the infrared). With an increased pump power of 1.6 mW, an additional pair is generated at 388.8 THz (771.6 nm) and 258.8 THz (1187 nm), as shown in the middle panel in Fig. 3(e). With a further increase in pump power to 2.5 mW, clustered combs are generated around the second signal–idler pair, while the first pair remains unaccompanied by other spectral tones [bottom panel in Fig. 3(e)].

These two OPO pairs measured in experiment agree quite well with the theoretical predictions [Fig. 3(d)], where pair I is predicted to be at 423 THz (I-s) and 221 THz (I-i) and pair II at 389 THz (II-s) and 255 THz (II-i). The m numbers of these modes are {420, 383, 310, 237, 200} for {I-s, II-s, p, II-i, I-i} [labeling scheme in Fig. 3(d)]. These mode numbers clearly satisfy phase matching ($\Delta m = 0$). Moreover, the fact that the clustered comb is generated in the II pair, but not in the I pair, is not coincidental and can be explained as follows. All the mode pairs satisfying phase matching are plotted in Fig. 3(d). Each mode is represented by an open circle, and the cavity free spectral range (FSR) is ≈ 1 THz. Although both I and II satisfy frequency matching, the densities of mode pairs (within a given range of frequency mismatch) around I and II are different. Because material dispersion is much larger at higher frequencies, the I pair exhibits larger dispersion and has sparser modes in the neighborhood of the tolerated frequency mismatch, which can be estimated by the cavity linewidth (≈ 300 MHz). In other words, the modes near II are preferred for clustered comb

generation considering both mode density and frequency matching. Moreover, because of the normal dispersion around the pump, there are no competitive processes in the pump band even at higher pump power [Fig. 3(e)]. A power-dependence study [Fig. 3(c)] indicates a threshold of (0.9 ± 0.1) mW for the first set of OPO lines. The second OPO has a threshold of (1.5 ± 0.2) mW, while its subsequent clustered frequency comb has a threshold near 2.5 mW.

For applications, the delivered output power of the OPO is an important metric. In our devices, the typical OPO signal and idler fields are 10 dB to 20 dB lower than the pump [Fig. 3(e)]. While this is actually better than previous widely separated OPO works (where the signal and idler are 30 dB to 50 dB lower than the pump [20,21]) and not uncommon for microcavity OPOs regardless of spectral separation (e.g., ≈ 15 dB difference in Ref. [32]), improving the conversion from pump to signal is nevertheless important. To do so, we anticipate that more advanced coupling engineering is needed to increase the out-coupling efficiency. While this will generally result in a higher threshold power, depending on the application, an appropriate balance can be struck between output power (e.g., for the visible wavelength signal) and overall power efficiency.

5. OPO ON A SINGLE WIDELY SEPARATED PAIR

In the previous section, although close-band OPO with spectral tones near the pump are successfully suppressed, the generation of two OPO pairs with pair II eventually exhibiting a cluster of tones might be unwanted in applications. Here we show how the ring geometry can be tuned to achieve a dispersion that supports only one single set of widely separated OPO tones.

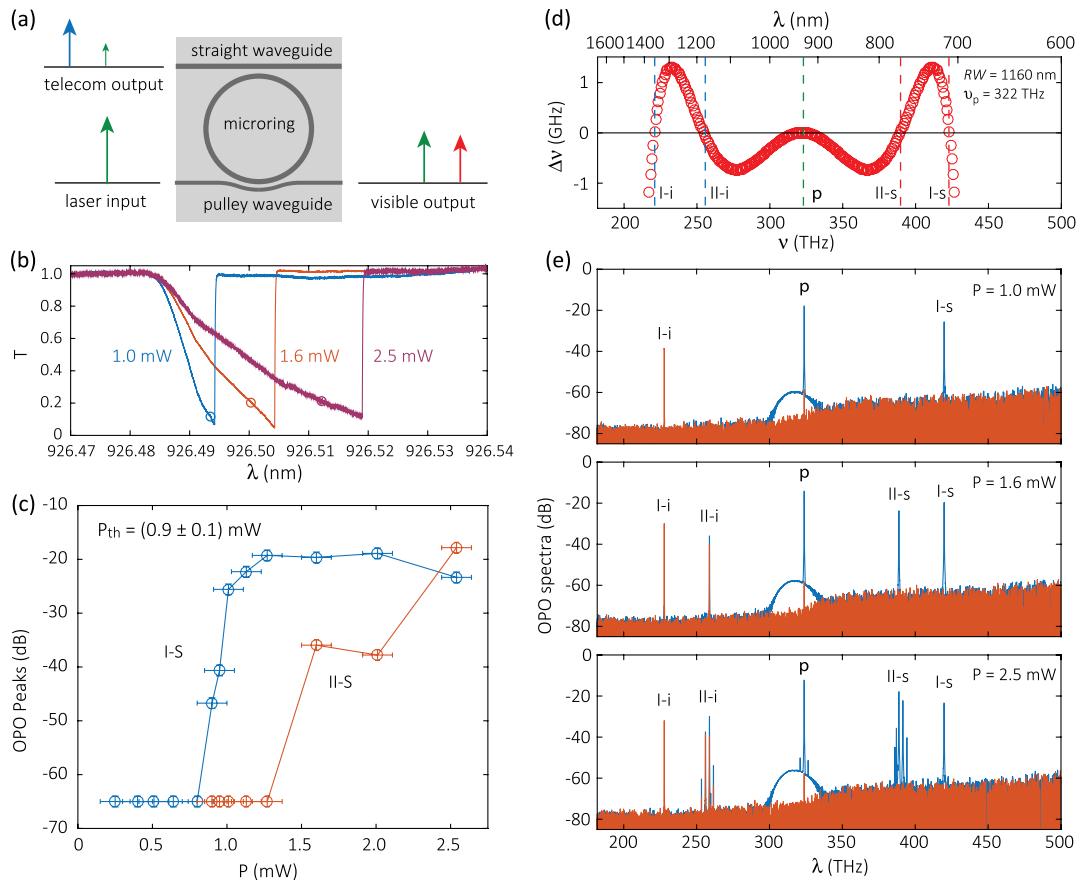


Fig. 3. Power dependence of the visible–telecom OPO. (a) When the OPO frequencies are separated widely into the visible–telecom regime, two waveguides are needed to couple the visible and telecom light efficiently. The straight waveguide (top) is used for out-coupling the telecom (idler), and the pulley waveguide (bottom) is for out-coupling the visible (signal). (b) Transmission (T) traces for $\nu_p \approx 322$ THz show bistabilities with various pump powers (P). The open circles specify the laser detuning at various powers for the OSA spectra in (e). (c) OPO threshold power is only (0.9 ± 0.1) mW, measured by the power dependence of the OPO signal peak amplitudes. I-s and II-s denote signal peaks of two OPO tones at 419.8 THz and 388.7 THz in (e). Here, on the y axis, 0 dB is referenced to 1 mW, i.e., dBm. Error bars are one standard deviation values due to fluctuations in optical path losses. The quoted pump power is on-chip, with the facet loss typically between 2 dB and 3 dB. (d) Zoom-in frequency mismatch curve of Fig. 1(d) suggests two phase/frequency-matched cases, where the signal/idler frequencies are labeled as I-s/I-i and II-s/II-i, respectively. The pump frequency is labeled as p (around 322 THz). (e) OPO spectra as a function of pump power. When the pump power is 1.0 mW, OPO I is above threshold and OPO II is below threshold, with I-s and I-i located around 419.8 THz (714.6 nm) and 227.8 THz (1316.9 nm), respectively, corresponding to a spectral separation of 192 THz. Next, when the pump power is 1.6 mW, both OPO I and II are above threshold and observable in the spectrum. II-s and II-i are located around 388.7 THz (771.8 nm) and 258.8 THz (1159.2 nm), respectively. The frequencies of both OPO I/II agree reasonably well with the theoretical prediction in (d). Finally, when the pump power is 2.5 mW, close-band FWM adjacent to OPO II is excited, because the modes adjacent to II have smaller frequency mismatch compared to those around I, as indicated by (d). On the y axis, 0 dB is referenced to 1 mW, i.e., dBm.

We calculate the device dispersion and OPO frequency mismatch for various ring widths using mode frequencies from finite-element method (FEM) simulations. The top panel in Fig. 4(a) shows the key result where the device with $RW = 1440$ nm is predicted to generate a visible–telecom OPO with signal and idler located at 384 THz (781 nm) and 204 THz (1470 nm), respectively, for a pump at 294 THz (1020 nm). This $H = 600$ nm design has widely separated frequency-/phase-matching mode pairs and normal dispersion near the pump, similar to the previous $H = 510$ nm design [Fig. 3(d)]. However, the $H = 600$ nm design supports only one widely separated OPO pair, and is also $\approx 5\times$ more dispersive in the frequency bands of interest. These two properties together make this design better in suppressing competitive OPO processes. In the measured optical spectrum [bottom panel in Fig. 4(a)], the fabricated device generates OPO with signal and idler at 383.9 THz (781.5 nm) and

202.1 THz (1484 nm), respectively, when pumping at 293.0 THz (1023.9 nm) with 1.3 mW pump drop power. The measured frequencies agree with theoretical prediction within 2 THz for all three modes. Moreover, only one pair of widely separated tones is generated, as the simulation predicts. We note that the short wavelength OPO output is suited for spectroscopy of rubidium vapor (1.5 nm wavelength tuning needed), and the telecom OPO output makes such a device potentially suitable for spectral translation [28]. We also note that in Fig. 4(c), a small close-to-pump OPO is generated at 1.5 mW pump drop power. Such close-band OPO is ≈ 10 dB smaller than the widely separated OPO and occurs only when the pump is depleted. The pump depletion effectively broadens the cavity linewidth (acts as another effective loss channel), thereby enabling the close-band OPO to occur.

One unique property of our device is its operation stability, i.e., OPO works at a continuous detuning of the pump. This

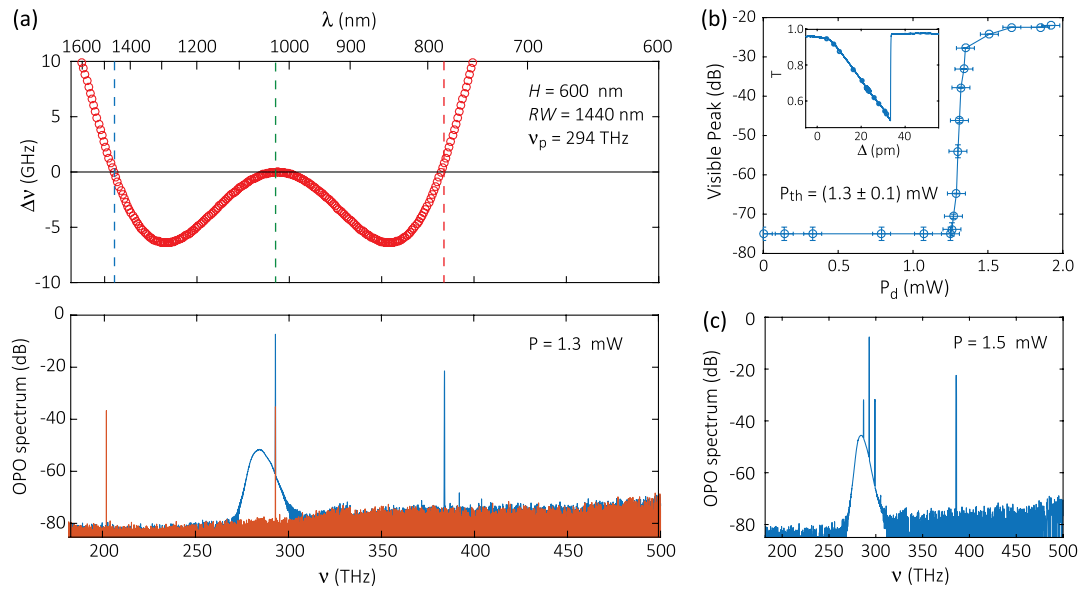


Fig. 4. OPO on a single widely separated pair. (a) Top panel shows a microring design with only one phase-/frequency-matched widely separated OPO pair. The microring has parameters of $H = 600$ nm and $RW = 1440$ nm. When the pump laser frequency $\nu_p = 293.5$ THz, the generated OPO is predicted to have only a single pair with frequencies of 205 THz and 382 THz. The bottom panel shows the experimental optical spectrum, which confirms that only a single widely separated pair is generated at 202.1 THz (1484 nm) and 383.9 THz (781.4 nm) when $\nu_p = 293.0$ THz (1024 nm). Due to the large spectral separation, the device needs two waveguides to couple the OPO signal and idler, with spectra shown in red and blue, respectively. (b) Threshold study of the OPO pair with various dropped pump powers $P_d = P(1 - T)$, where transmission (T) is changed by the laser-cavity detuning (Δ), as shown in the inset. The threshold power is (1.3 ± 0.1) mW. (c) Dispersion is normal near the pump, as shown in (a), thereby disfavoring close-band OPO. However, when the pump power is sufficiently above threshold, the close-band OPO process begins to appear. This competitive OPO is much less efficient than the widely separated OPO, but nevertheless needs further suppression for ideal operation. In the y axes of (b) and (c), 0 dB is referenced to 1 mW, i.e., dBm.

stability has not been demonstrated in prior works, where large pump power is used to assist phase matching, and clean OPO pairs typically require sensitive pump detuning. For example, in Ref. [20], a cluster frequency comb is clearly in competition with the clean OPO pair when the detuning changes. In contrast, our OPO has stable output frequencies. We study this stability by recording the peak amplitude of the 781.5 nm signal versus the pump power dropped inside the microring [Fig. 4(b), inset]. The pump threshold power is (1.3 ± 0.1) mW, similar to, but slightly larger than, that of the previous design. In particular, we observe only one widely separated OPO pair throughout this detuning process, until at the highest dropped powers, one close-band OPO occurs [Fig. 4(c)]. Importantly, such close-band OPO, although affecting the output power for the targeted widely-separated OPO, does not come with clustered frequency combs near the signal and idler. We note that an advanced coupling design can help suppress the close-band OPO (see Supplement 1 for details).

The stability can be attributed to three factors. First, our device has a smaller size and thus a FSR of ≈ 1 THz, whereas Ref. [21] has a larger size and a FSR of ≈ 100 GHz to 300 GHz. Second, because of the larger material dispersion at the visible wavelength and larger geometric dispersion of the nanophotonic devices, the modes around OPO pairs are more dispersive and therefore less prone to clustered frequency combs. More importantly, our devices have smaller operation powers and thus smaller parametric gain bandwidths, which further limits the allowable number of competitive OPO processes. Such superior power efficiency and operation stability comes with a sacrifice of frequency tunability. For example, our results typically show only a few pump modes that can generate widely separated OPO, as shown in Fig. 2(b),

while previous works possess $\approx 10\times$ more pump modes for such operation [21]. We note that the frequency tunability can be aided with pump power tuning but not temperature tuning (Supplement 1).

6. CONCLUSION

In summary, we propose and demonstrate, for the first time, visible–telecom OPO using silicon nanophotonics, with a signal–idler spectral separation of ≈ 190 THz, and a sub-mW threshold power that is two orders of magnitudes smaller than recently reported infrared OPO [21]. Our demonstration represents a major advance for the on-chip generation of coherent visible light. Compatibility with silicon photonics and its accompanying potential for low-cost, scalable fabrication make our approach particularly promising for integrated photonics applications.

Funding. Defense Advanced Research Projects Agency (DODOS); NIST-University of Maryland (70NANB10H193); National Institute of Standards and Technology (NIST-on-a-chip).

Acknowledgment. X.L., G. M., Q.L., and A.S. acknowledge support under the Cooperative Research Agreement between the University of Maryland and NIST-PML.

See Supplement 1 for supporting content.

REFERENCES

1. M. T. Hummon, S. Kang, D. G. Bopp, Q. Li, D. A. Westly, S. Kim, C. Fredrick, S. A. Diddams, K. Srinivasan, V. Aksyuk, and J. E. Kitching, "Photonic chip for laser stabilization to an atomic vapor with 10^{-11} instability," *Optica* **5**, 443–449 (2018).
2. A. D. Ludlow, M. M. Boyd, J. Ye, E. Peik, and P. O. Schmidt, "Optical atomic clocks," *Rev. Mod. Phys.* **87**, 637–701 (2015).
3. Y. Sun, K. Zhou, Q. Sun, J. Liu, M. Feng, Z. Li, Y. Zhou, L. Zhang, D. Li, S. Zhang, M. Ikeda, S. Liu, and H. Yang, "Room-temperature continuous-wave electrically injected InGaN-based laser directly grown on Si," *Nat. Photonics* **10**, 595–599 (2016).
4. R. W. Boyd, *Nonlinear Optics* (Academic, 2008).
5. G. Agrawal, *Nonlinear Fiber Optics* (Academic, 2007).
6. J. A. Giordmaine and R. C. Miller, "Tunable coherent parametric oscillation in LiNbO₃ at optical frequencies," *Phys. Rev. Lett.* **14**, 973–976 (1965).
7. M. Ebrahimzadeh, M. H. Dunn, and F. Akerboom, "Highly efficient visible urea optical parametric oscillator pumped by a XECL excimer laser," *Opt. Lett.* **14**, 560–562 (1989).
8. P. F. Moulton, "Spectroscopic and laser characteristics of Ti:Al₂O₃," *J. Opt. Soc. Am. B* **3**, 125–133 (1986).
9. A. Y. H. Chen, G. K. L. Wong, S. G. Murdoch, R. Leonhardt, J. D. Harvey, J. C. Knight, W. J. Wadsworth, and P. St. J. Russell, "Widely tunable optical parametric generation in a photonic crystal fiber," *Opt. Lett.* **30**, 762–764 (2005).
10. Y. Deng, Q. Lin, F. Lu, G. P. Agrawal, and W. H. Knox, "Broadly tunable femtosecond parametric oscillator using a photonic crystal fiber," *Opt. Lett.* **30**, 1234–1236 (2005).
11. Q. Lin, T. J. Johnson, R. Perahia, C. P. Michael, and O. J. Painter, "A proposal for highly tunable optical parametric oscillation in silicon micro-resonators," *Opt. Express* **16**, 10596–10610 (2008).
12. J. S. Levy, M. A. Foster, A. L. Gaeta, and M. Lipson, "Harmonic generation in silicon nitride ring resonators," *Opt. Express* **19**, 11415–11421 (2011).
13. X. Guo, C.-L. Zou, and H. X. Tang, "Second-harmonic generation in aluminum nitride microrings with 2500%/W conversion efficiency," *Optica* **3**, 1126–1131 (2016).
14. J. Lin, Y. Xu, J. Ni, M. Wang, Z. Fang, L. Qiao, W. Fang, and Y. Cheng, "Phase-matched second-harmonic generation in an on-chip LiNbO₃ microresonator," *Phys. Rev. Appl.* **6**, 014002 (2016).
15. S. Fujii, T. Kato, R. Suzuki, and T. Tanabe, "Third-harmonic blue light generation from Kerr clustered combs and dispersive waves," *Opt. Lett.* **42**, 2010–2013 (2017).
16. T. Carmon and K. J. Vahala, "Visible continuous emission from a silica microphotonic device by third-harmonic generation," *Nat. Phys.* **3**, 430–435 (2007).
17. J. B. Surya, X. Guo, C.-L. Zou, and H. X. Tang, "Efficient third-harmonic generation in composite aluminum nitride/silicon nitride microrings," *Optica* **5**, 103–108 (2018).
18. L. Chang, A. Boes, P. Pintus, J. D. Peters, M. J. Kennedy, X.-W. Guo, N. Volet, S. Yu, S. B. Papp, and J. E. Bowers, "High efficiency SHG in heterogenous integrated GaAs ring resonators," *APL Photon.* **4**, 036103 (2019).
19. N. L. B. Sayson, K. E. Webb, S. Coen, M. Erkintalo, and S. G. Murdoch, "Widely tunable optical parametric oscillation in a Kerr microresonator," *Opt. Lett.* **42**, 5190–5193 (2017).
20. S. Fujii, S. Tanaka, M. Fuchida, H. Amano, Y. Hayama, R. Suzuki, Y. Kakinuma, and T. Tanabe, "Octave-wide phase-matched four-wave mixing in dispersion engineered crystalline microresonators," *Opt. Lett.* **44**, 3146–3149 (2019).
21. N. L. B. Sayson, T. Bi, V. Ng, H. Pham, L. S. Trainor, H. G. L. Schwefel, S. Coen, M. Erkintalo, and S. G. Murdoch, "Octave-spanning tunable parametric oscillation in crystalline Kerr microresonators," *Nat. Photonics* **13**, 701–707 (2019).
22. D. J. Moss, R. Morandotti, A. L. Gaeta, and M. Lipson, "New CMOS-compatible platforms based on silicon nitride and hydex for nonlinear optics," *Nat. Photonics* **7**, 597–607 (2013).
23. Y. Okawachi, K. Saha, J. S. Levy, Y. H. Wen, M. Lipson, and A. L. Gaeta, "Octave-spanning frequency comb generation in a silicon nitride chip," *Opt. Lett.* **36**, 3398–3400 (2011).
24. Q. Li, T. C. Briles, D. A. Westly, T. E. Drake, J. R. Stone, B. R. Ilic, S. A. Diddams, S. B. Papp, and K. Srinivasan, "Stably accessing octave-spanning microresonator frequency combs in the soliton regime," *Optica* **4**, 193–203 (2017).
25. M. Karpov, M. H. Pfeiffer, J. Liu, A. Lukashchuk, and T. J. Kippenberg, "Photonic chip-based soliton frequency combs covering the biological imaging window," *Nat. Commun.* **9**, 1146 (2018).
26. Q. Li, M. Davanço, and K. Srinivasan, "Efficient and low-noise single-photon-level frequency conversion interfaces using silicon nanophotonics," *Nat. Photonics* **10**, 406–414 (2016).
27. A. Singh, Q. Li, S. Liu, Y. Yu, X. Lu, C. Schneider, S. Höfling, J. Lawall, V. Verma, R. Mirin, S. W. Nam, J. Liu, and K. Srinivasan, "Quantum frequency conversion of a quantum dot single-photon source on a nanophotonic chip," *Optica* **6**, 563–569 (2019).
28. X. Lu, G. Moille, Q. Li, D. A. Westly, A. Rao, S.-P. Yu, T. C. Briles, S. B. Papp, and K. Srinivasan, "Efficient telecom-to-visible spectral translation using silicon nanophotonics," *Nat. Photonics* **13**, 593–601 (2019).
29. X. Lu, Q. Li, D. A. Westly, G. Moille, A. Singh, V. Anant, and K. Srinivasan, "Chip-integrated visible-telecom photon pair sources for quantum communication," *Nat. Phys.* **15**, 373–381 (2019).
30. A. B. Matsko, A. A. Savchenkov, S.-W. Huang, and L. Maleki, "Clustered frequency comb," *Opt. Lett.* **41**, 5102–5105 (2016).
31. S.-W. Huang, A. K. Vinod, J. Yang, M. Yu, D.-L. Kwong, and C. W. Wong, "Quasi-phase-matched multispectral Kerr frequency comb," *Opt. Lett.* **42**, 2110–2113 (2017).
32. T. J. Kippenberg, S. Spillane, and K. J. Vahala, "Kerr-nonlinearity optical parametric oscillation in an ultrahigh-Q toroid microcavity," *Phys. Rev. Lett.* **93**, 083904 (2004).
33. X. Lu, S. Rogers, W. C. Jiang, and Q. Lin, "Selective engineering of cavity resonance for frequency matching in optical parametric processes," *Appl. Phys. Lett.* **105**, 151104 (2014).